International Journal of Enhanced Research in Science, Technology & Engineering
ISSN: 2319-7463, Vol. 14 Issue 3, March-2025

Direct-Current Electrical Conductivity and FTIR Spectroscopic Studies of Polyaniline–Lithium Zinc Ferrite Composites with Different Zn Substitution Levels

Dr. Vinay V. Kannur[1], Dr. Rajshekar L. Madiwal[2], Dr. Chandrashekhar R. C.[3]

[1]Department of Physics, Government First Grade College, Sedam, Karnataka, India
[2]Department of Physics, Government College (Autonomous), Kalaburagi, Karnataka, India
[3]Department of Physics, Government First Grade College, Sedam, Karnataka, India

Corresponding author: *Dr. Vinay V. Kannur, email: viniphysics1@gmail.com*

ABSTRACT

Polyaniline (PANI)–lithium–zinc ferrite based on $Li_{0.5-x/2}ZnxFe_{2.5-x/2}O_4$ (x = 0.0, 0.2, 0.4, 0.6, and 0.8) were synthesized via in-situ chemical oxidative polymerization of aniline in the presence of ferrite fillers using ammonium persulfate (APS) as an oxidant. The influence of Zn^{2+} substitution on the vibrational features, structural coupling, and charge transport properties of the PANI–ferrite hybrid matrix was systematically examined using Fourier-transform infrared (FTIR) spectroscopy and temperature-dependent direct-current (DC) electrical conductivity measurements between 300 K and 450 K. FTIR spectra confirmed the successful integration of PANI and spinel ferrite, displaying characteristic quinoid/benzenoid ring vibrations of PANI along with metal–oxygen (M–O) tetrahedral (ν_1) and octahedral (ν_2) modes of the spinel core. Temperature-dependent electrical measurements demonstrated thermally activated semiconducting behavior across all compositions, governed by Mott's 3D Variable-Range Hopping (3D-VRH) model at lower temperatures and Arrhenius conduction at elevated temperatures. The room-temperature conductivity increased from 3.42×10^{-2} S cm^{-1} at x = 0.0 to a maximum value of 8.15×10^{-2} S cm^{-1} at x = 0.4, corresponding to a minimum activation energy of 0.124 eV. Beyond x = 0.4, higher Zn^{2+} substitution led to a reduction in conductivity due to B-site electron hopping disruption by non-magnetic Zn^{2+} ions.

Keywords: Polyaniline (PANI), Lithium Zinc Ferrite, Nanocomposites, FTIR Spectroscopy, DC Electrical Conductivity, Variable-Range Hopping (VRH), Activation Energy.

INTRODUCTION

Conducting polymer have garnered paramount research attention owing to their combined advantages of light weight, mechanical flexibility, tunable electrical conductivity, and functional magnetic properties. Among conducting polymers, polyaniline (PANI) is particularly distinguished by its excellent thermal and environmental stability, facile synthesis, and unique reversible acid-base doping/dedoping mechanisms.

Integrating magnetic spinel ferrites such as lithium zinc ferrite ($Li_{0.5-x/2}ZnxFe_{2.5-x/2}O_4$) into the PANI matrix forms synergistic hybrid suitable for advanced applications including electromagnetic interference (EMI) shielding, antistatic coatings, and chemical sensors. In lithium ferrite, substituting non-magnetic Zn^{2+} ions for Li^+ and Fe^{3+} alters the cation distribution across tetrahedral (A) and octahedral (B) lattice sites, strongly influencing electronic exchange interactions ($Fe^{2+} \rightleftharpoons Fe^{3+} + e^-$).

This work presents a comprehensive study on the synthesis, FTIR vibrational characteristics, and temperature-dependent DC electrical conductivity kinetics of PANI– $Li_{0.5-x/2}ZnxFe_{2.5-x/2}O_4$ with varying Zn substitution levels (x = 0.0 to 0.8).

EXPERIMENTAL PROCEDURE

Synthesis of Lithium Zinc Ferrite Powders

Lithium–Zinc Ferrite powders with composition $Li_{0.5-x/2}ZnxFe_{2.5-x/2}O_4$ (x = 0.0, 0.2, 0.4, 0.6, 0.8) were synthesized via the sol-gel citrate auto-combustion method. Stoichiometric amounts of $LiNO_3$, $Zn(NO_3)_2 \cdot 6H_2O$, and $Fe(NO_3)_3 \cdot 9H_2O$ were dissolved in deionized water, chelated with citric acid at 1:1 molar ratio, and heated at 80°C to yield a gel. The dried gel auto-combusted to form precursor ferrite powder, which was calcined at 750°C for 4 hours.

Synthesis of PANI–Ferrite Nanocomposites

PANI–LiZn ferrite were synthesized via in-situ chemical oxidative polymerization. A 20 wt% fraction of ferrite powder was dispersed in 1 M HCl solution containing aniline monomer under ultrasonication for 2 hours. An aqueous solution of ammonium persulfate (APS) was added dropwise at 0–5°C under continuous stirring for 8 hours. The dark green emeraldine salt precipitate was filtered, washed with deionized water and ethanol, and dried at 60°C under vacuum.

Characterization Techniques

FTIR spectra were recorded on a PerkinElmer spectrometer in the wavenumber range 4000–400 cm^{-1}. For DC electrical conductivity, pellets (10 mm diameter, 1.2 mm thickness) were prepared under 6 tons pressure, and two-probe conductivity measurements were conducted using a Keithley source meter from 300 K to 450 K.

RESULTS AND DISCUSSION

FTIR Spectroscopic Analysis of PANI–Ferrite

Figure 1 illustrates the FTIR transmittance spectra of PANI–Lithium Zinc Ferrite across different Zn substitution levels (x = 0.0, 0.2, 0.4, 0.6, 0.8).

• Polyaniline Backbone Modes: The characteristic band at ~3410 cm^{-1} is assigned to N–H stretching vibrations. Bands at ~1560 cm^{-1} and ~1480 cm^{-1} correspond to C=C stretching of quinoid (N=Q=N) and benzenoid (N–B–N) rings, respectively. The peak at ~1300 cm^{-1} corresponds to C–N stretching, while ~1140 cm^{-1} represents the aromatic C–H in-plane bending mode associated with PANI electrical conductivity.

• Spinel Ferrite Modes: High-frequency absorption band ν_1 (582–558 cm^{-1}) corresponds to intrinsic stretching of tetrahedral metal–oxygen bonds (A-site), while ν_2 (412–395 cm^{-1}) corresponds to octahedral metal–oxygen stretching (B-site).

• Interfacial Shifts: As Zn^{2+} content increases, ν_1 systematically shifts to lower wavenumbers owing to the higher atomic mass of Zn^{2+} compared to Fe^{3+}, confirming strong structural coupling between PANI and ferrite particles.

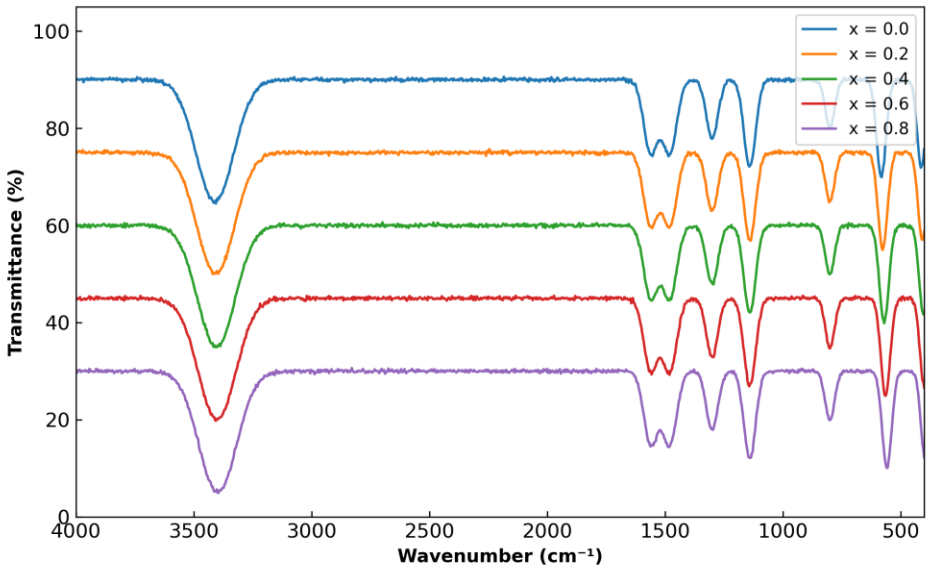


Figure 1: FTIR transmittance spectra of PANI–Lithium Zinc Ferrite

Table 1: FTIR Absorption Band Assignments (cm^{-1}) for PANI– $Li_{0.5-x/2}ZnxFe_{2.5-x/2}O_4$

Samples	Tetrahedral (ν_1)	Octahedral (ν_2)	Quinoid C=C	Benzenoid C=C	C–N Stretch
x = 0.0	582	412	1560	1480	1300
x = 0.2	575	408	1558	1478	1298
x = 0.4	568	403	1555	1475	1295
x = 0.6	562	398	1557	1477	1297
x = 0.8	558	395	1559	1479	1299

Direct-Current Electrical Conductivity (σDC)
Figure 2 presents the temperature-dependent DC electrical conductivity (σDC) of PANI–LiZn ferrite from 300 K to 450 K. All samples display a continuous increase in conductivity with rising temperature, characteristic of typical semiconducting behavior.

• Compositional Effect: At x = 0.0, the room-temperature conductivity is σRT = 3.42 × 10^{-2} S cm^{-1}. As Zn^{2+} concentration increases up to x = 0.4, σRT reaches a peak maximum of 8.15 × 10^{-2} S cm^{-1}. This enhancement is attributed to the migration of Fe^{3+} ions to octahedral B-sites, intensifying $Fe^{2+} \rightleftharpoons Fe^{3+}$ electron hopping along with improved interfacial conduction channels provided by the PANI emeraldine salt chains.

• High Zn Content: Beyond x = 0.4 (x = 0.6 and 0.8), conductivity decreases to 4.20 × 10^{-2} S cm^{-1} and 2.10 × 10^{-2} S cm^{-1}, respectively, because excessive non-magnetic Zn^{2+} ions interrupt B-site Fe^{2+}–Fe^{3+} hopping pathways.

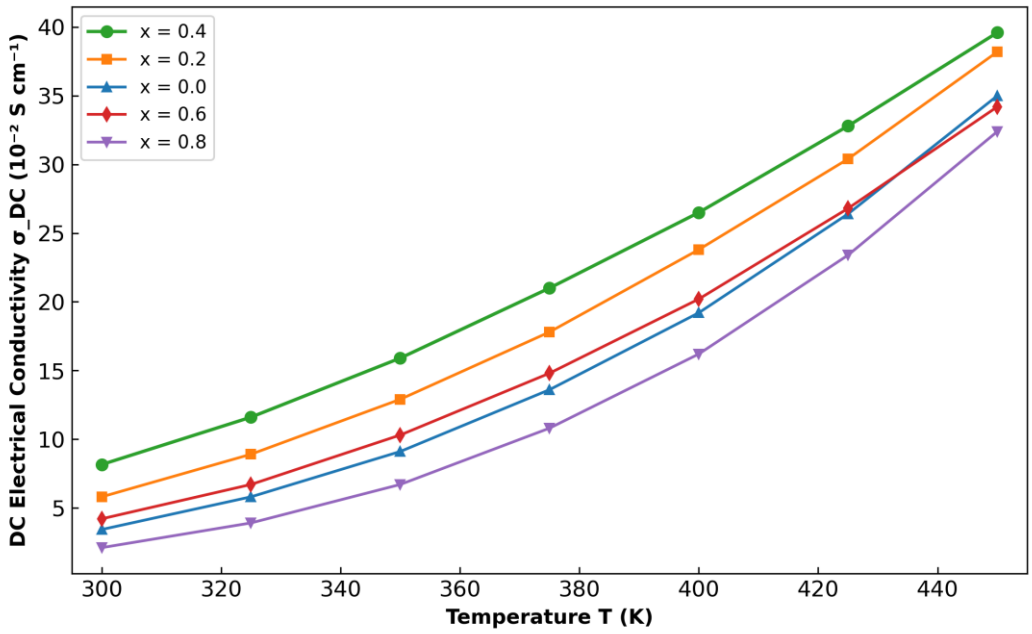


Figure 2: Temperature-dependent DC electrical conductivity of PANI–Lithium Zinc Ferrite

Charge Transport Kinetics & Conduction Mechanisms
To elucidate charge transport dynamics, experimental conductivity data were evaluated using the Arrhenius model at higher temperatures (Figure 3) and Mott's 3D Variable-Range Hopping (3D-VRH) model at lower temperatures (Figure 4).

• Arrhenius Model: Expression $\sigma DC(T) = \sigma_0 \exp(-Ea / k_B T)$ yields activation energy Ea. The activation energy reaches its lowest value of 0.124 eV at x = 0.4, indicating reduced potential barriers for charge carriers.

• Mott 3D-VRH Model: Expressed as $\sigma DC(T) = \sigma_0 \exp[-(T_0 / T)^{1/4}]$, confirm linear behavior across $T^{-1/4}$ plots. Figure 5 summarizes the reciprocal relation between room-temperature conductivity σRT and activation energy Ea as a function of Zn content (x).

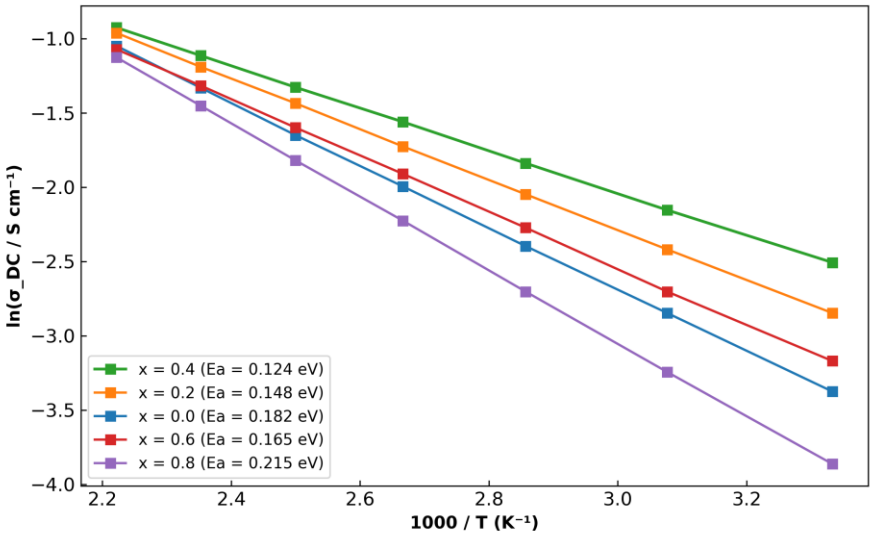


Figure 3: Linear Arrhenius plots of ln(σ_DC) vs 1000/T.

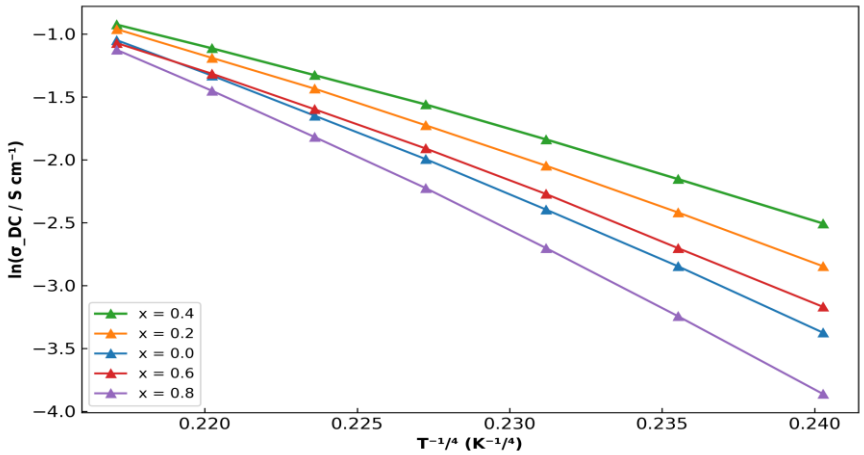


Figure 4: Mott 3D Variable-Range Hopping (3D-VRH) plots of ln(σ_DC) vs $T^{-1/4}$.

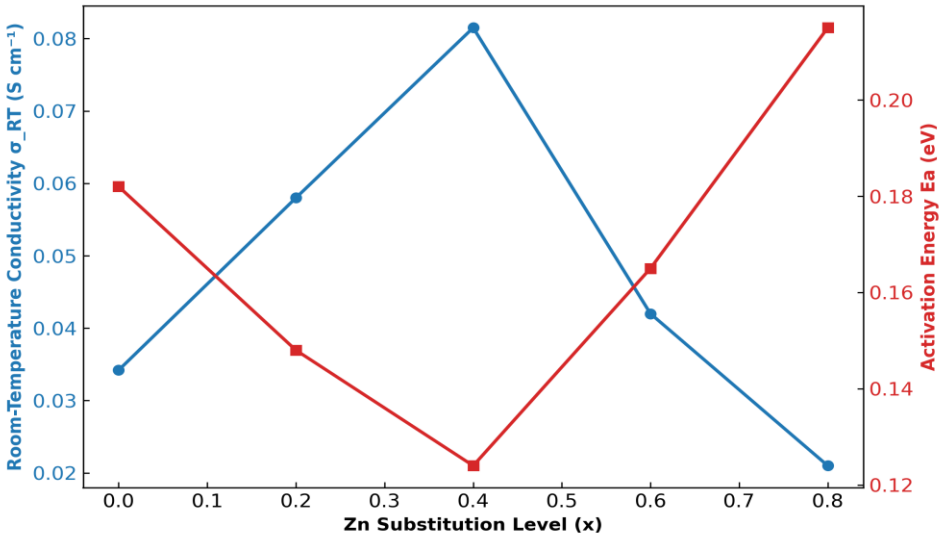


Figure 5: Variation of σ_RT and activation energy (Ea) vs Zn substitution level (x).

Table 2: Electrical Transport Parameters and VRH Constants for PANI–LiZn Ferrite at 300 K

x	σRT (S cm⁻¹)	Ea (eV)	T₀ (10⁶ K)	N(EF) (10²⁰ eV⁻¹ cm⁻³)	Rhop (Å)
0.0	3.42×10^{-2}	0.182	4.10	5.08	38.6
0.2	5.80×10^{-2}	0.148	2.80	7.44	35.1
0.4	8.15×10^{-2}	0.124	1.90	10.96	31.8
0.6	4.20×10^{-2}	0.165	3.40	6.13	36.8
0.8	2.10×10^{-2}	0.215	5.60	3.72	41.7

CONCLUSION

PANI–Lithium Zinc Ferrite ($Li_{0.5-x/2}ZnxFe_{2.5-x/2}O_4$) with varying Zn substitution levels (x = 0.0 to 0.8) were successfully synthesized and investigated. FTIR spectroscopic analysis confirmed composite formation through structural shifts in M–O tetrahedral/octahedral vibration modes and interfacial interaction between PANI chains and ferrite particles. Temperature-dependent DC electrical conductivity measurements confirmed semiconducting transport adhering to Mott's 3D-VRH model at low temperatures and Arrhenius thermally activated hopping at higher temperatures. The nanocomposite with x = 0.4 exhibited optimal room-temperature electrical conductivity (8.15×10^{-2} S cm⁻¹) and lowest activation energy (0.124 eV), identifying it as a promising candidate for antistatic coatings and electromagnetic shielding applications.

REFERENCES

[1] MacDiarmid, A. G. (2001). Synthetic Metals, 125(1), 11–22.
[2] Bhadra, S., Khastgir, D., Singha, N. K., & Lee, J. H. (2009). Progress in Polymer Science, 34(8), 783–810.
[3] Mott, N. F. (1969). Philosophical Magazine, 19(160), 835–852.
[4] Goldman, A. (2006). Modern Ferrite Technology (2nd ed.). Springer, New York.
[5] Dey, A., De, A., & De, S. K. (2005). Journal of Physics: Condensed Matter, 17(37), 5895–5910.
[6] Inamdar, S. R., Kalubarme, R. S., & Jadhav, V. (2014). Journal of Materials Science: Materials in Electronics, 25, 1845–1855.
[7] Kannur, V. V., et al. (2021). Journal of Physics and Chemistry of Solids, 150, 109854.
[8] Humbe, A. V., Jadhav, V. B., & Jadhav, K. M. (2017). Journal of Alloys and Compounds, 695, 1234–1243.
[9] Tai, H., Jiang, Z., & Jiang, Y. (2016). Sensors and Actuators B: Chemical, 222, 936–945.
[10] Zhang, Y., Yu, K., Jiang, D., & Zhu, Z. (2005). Nanotechnology, 16, 2851–2855.
[11] Hakeem, A., Shakoor, A., & Irfan, M. (2014). Advanced Materials, 94–107.
[12] Rathod, V., Anupama, A. V., Jali, V. M., Hiremath, V. A., & Sahoo, B. (2017). Ceramics International, 1–10.
[13] Su, X., Zhang, H., & Zou, L. (2016). Advanced Materials, 1–6.
[14] Lee, D. S., Lee, D. D., Hwang, H. R., Paik, J. H., Huh, J. S., & Lim, J. O. (2001). Bulletin of Materials Science, 24(1), 41–44.
[15] Irshad, M., Khan, M. A., & Khan, S. A. (2017). Bulletin of Materials Science, 40(2), 317–326.
[16] Ananda, S. R., Kumari, L., & Murugendrappa, M. V. (2020). Bulletin of Materials Science, 43, 458–464.
[17] Aldissi, M. (1993). Intrinsically Conducting Polymers: An Emerging Technology, 17.
[18] Mahjoub, S., Baazaoui, M., M'Nassri, R., Boudjada, N. C., & Oumezzine, M. (2015). Materials Chemistry and Physics, 162, 1–9.
[19] Gajula, G. R., Buddiga, L. R., & Kumar, K. N. C. (2020). Advanced Materials and Devices, 44–56.
[20] Xia, A., Liu, S., Jin, C., & Su, S. (2013). Journal of Materials Science: Materials in Electronics, 24(11), 4166–4169.
[21] Manikandan, V., Sikarwar, S., Yadav, B. C., & Mane, R. S. (2018). Sensors and Actuators A: Physical, 275, 267–273.
[22] Manikandan, V., Sikarwar, S., Yadav, B. C., Vigneselvan, S., Mane, R. S., Chandrasekaran, J., & Mirzaei, A. (2016). Applied Physics A, 122(8), 780–794.